PCCP

RSC Publishing

PAPER

View Article Online
View Journal | View Issue

Cite this: *Phys. Chem. Chem. Phys.*, 2013, **15**, 18906

Thermodynamics of native point defects in α-Fe_2O_3: an *ab initio* study

Joohee Lee and Seungwu Han*

Received 4th August 2013,
Accepted 20th September 2013

DOI: 10.1039/c3cp53311e

www.rsc.org/pccp

The native point defects in Fe_2O_3 are theoretically investigated using *ab initio* methods based on the GGA + *U* formalism. We consider vacancies and interstitials of Fe and O atoms as well as the electron polaron as Fe^{II} defects at the host Fe^{III} site. The formation energies and charge transition levels are computed for each defect type with careful elimination of size effects of the supercell. It is found that the Fe interstitial and vacancy form donor and acceptor levels close to band edges, respectively, thereby allowing for charge carriers at room temperature. We determine the oxygen deficiency under high-temperature equilibrium conditions and find an excellent agreement with experiment. In the quenched condition, it is found that the Fermi level is pinned at ~0.5 eV below the conduction band minimum, which may limit the performance of Fe_2O_3 as a photoanode in solar water-splitting cells. Furthermore, the oxygen vacancy is mostly neutral and the Fe interstitial is responsible for electron carriers.

1 Introduction

The corundum-structured ferric oxide, α-Fe_2O_3 (simply Fe_2O_3 in the present work) or hematite, has been receiving a good deal of recent attention as a material for photoanodes in photoelectrochemical (PEC) cells for water splitting owing to several advantages such as the energy gap lying in the visible spectrum, valence edge below the water-oxidation level, and low material costs.[1] However, the short diffusion length of holes in Fe_2O_3 is known to prohibit the efficient charge separation.[2] To improve the material properties, several attempts have been made. For example, dopants were introduced to increase the carrier concentration in an extrinsic way,[3,4] or nanostructures were employed to shorten the diffusion length between the photogenerated holes and the surface.[1,2,5]

Recently, it was also reported that the PEC performance of Fe_2O_3 is significantly enhanced through defect engineering.[6–8] The defects were introduced during the material synthesis in an oxygen-deficient environment[6] or by high-intensity ultrasonication.[8] It was suggested that the donor density was increased due to the formation of oxygen vacancies (V_O), improving the photoactivity.[6] In fact, the enhancement of PEC performance by increasing the density of native defects has been also reported for other metal-oxide nanostructures such as TiO_2 nanowires.[7,9]

In spite of the growing importance of Fe_2O_3 in practical applications, the fundamental understanding of the native defects in Fe_2O_3 is not satisfactory yet. Experimentally, the defect study on hematite dates back to as early as 1960s.[10–14] The main focus of these studies was on the electrical properties of non-stoichiometric $Fe_2O_{3-\delta}$ grown at relatively high temperatures with various oxygen partial pressures (p_{O_2}). From the dependence of oxygen deficiency on the partial pressure, it was evidenced that V_O is the dominant native defect between 1100 and 1300 °C.[11]

Theoretically, there have been a few computational investigations on the defect properties of Fe_2O_3 using the classical potentials.[15,16] However, considering the complex nature of multivalent oxides such as Fe_2O_3, a detailed study at the *ab initio* level is highly desirable. There have been *ab initio* studies on the bulk properties of Fe_2O_3 (ref. 17–19) but no work has been reported on the defect properties as far as we are aware of. In the present work, we study the intrinsic point defects in Fe_2O_3 using the *ab initio* methods based on the density functional theory. We consider both vacancy and interstitial defects such as V_O, Fe vacancy (V_{Fe}), interstitial O (O_I) and interstitial Fe (Fe_I) atoms, and focus on the defect levels within the band gap and their influence on electrical properties. We also investigate the formation energies to estimate the equilibrium defect densities at a given temperature and p_{O_2}.

2 Computational details

We carry out *ab initio* calculations using the Vienna *Ab initio* Simulation Package (VASP) code[20] based on the projector-augmented wave (PAW) pseudopotential.[21] To address the electron correlation within Fe d orbitals, we employ the rotationally

Department of Materials Science and Engineering and Research Institute of Advanced Materials, Seoul National University, Seoul 151-755, South Korea. E-mail: hansw@snu.ac.kr

invariant form of the GGA + U functional.[22] Therefore, the model Hamiltonian describing the on-site interaction depends only on $U-J$, where U and J correspond to the on-site Coulomb and exchange parameters, respectively. In the present work, $U-J$ or the effective U parameter of 4.3 eV is used.[18] The valence electron configuration of $4s^1 3d^7$ and $2s^2 2p^4$ are considered for Fe and O atoms. The cutoff energy for the plane-wave basis set is chosen to be 550 eV, and the k-space mesh grid of $4 \times 4 \times 4$ is used for the primitive cell. These parameters ensure the energy convergence to be within 10 meV per atom. The ionic configurations are relaxed until the magnitudes of atomic forces of all ions are less than 0.02 eV $Å^{-1}$. For defect calculations, the hexagonal unit cell is expanded by $2 \times 2 \times 1$ containing 120 atoms plus a defect, except for the case of Fe_I where the rhombohedral primitive cell is expanded by $3 \times 3 \times 2$ with 180 atoms to isolate more extended defect states. The $2 \times 2 \times 2$ k points are sampled in the defective supercells.

3 Results

3.1 Bulk property

Fe_2O_3 is a corundum-structured oxide like Al_2O_3 in which Fe ions occupy two thirds of octahedral interstitial sites. Fe_2O_3 is known to be antiferromagnetic at low temperatures and becomes canted antiferromagnetic or weakly ferromagnetic above 250 K (so called Morin transition).[23] Above Néel temperature (about 960 K), Fe_2O_3 becomes paramagnetic. We consider various spin configurations of Fe atoms and the minimum energy is obtained when the magnetic moments of Fe atoms are aligned in parallel within the *ab* plane but alternate along the *c* axis (see Fig. 1a). This is consistent with other works.[24–26] The basic bulk properties computed within the present computational setup are compiled in Table 1. The agreements with experiment and previous theoretical work are reasonable.

The partial density of states (PDOS) of Fe_2O_3 is shown in Fig. 1b, which shows that the valence band is a mixture of O p and majority Fe d orbitals while the conduction band comprises mostly minority Fe d orbitals. This means that the energy gap of Fe_2O_3 is of the charge-transfer type as was confirmed by photoemission experiments.[27,28] We also decompose Fe d orbitals into t_{2g} and e_g orbitals and the energy ordering in Fig. 1b is consistent with the well-known crystal field theory.[29]

3.2 Electronic structures of neutral defects

Next, we examine the change in the local atomic and electronic structures when each type of point defect is introduced with the neutral charge state.

3.2.1 Oxygen vacancy (V_O). The oxygen atoms in Fe_2O_3 are bonded with four Fe atoms in the upper and lower Fe layers (see Fig. 2a). In the crystalline structure, Fe–O bond lengths are 2.12 and 1.97 Å (denoted as Fe (long) and Fe (short) in Fig. 2a). When the oxygen atom is removed, neighboring Fe (O) atoms relax outward (inward) by $\sim$0.15 ($\sim$0.1) Å.

In Fig. 2b, it is seen that the oxygen vacancy gives rise to three defect levels (α, β, and γ) within the band gap of the spin-symmetric DOS. The α state is distributed rather broadly over

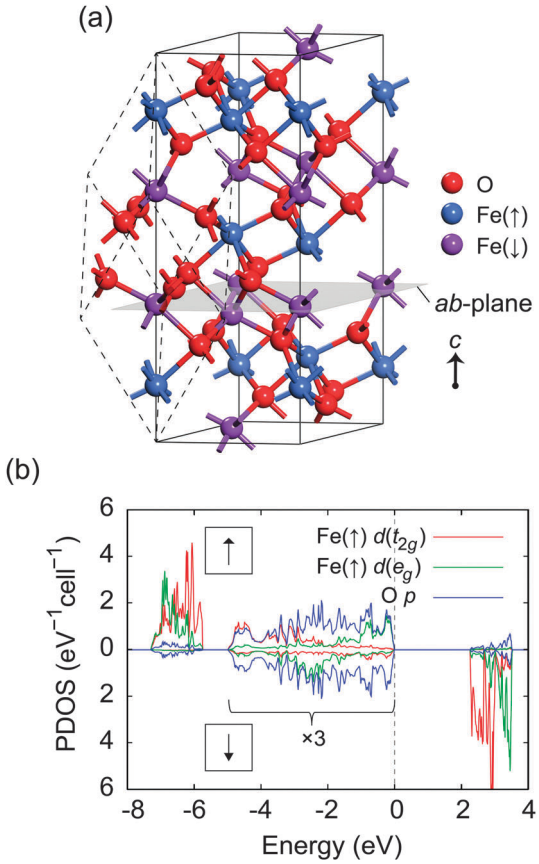

Fig. 1 (a) The crystal structure of Fe_2O_3. The rhombohedral primitive cell and the hexagonal conventional cell are indicated by the dashed and solid lines, respectively. The magnetic configuration of Fe atoms is also shown. (b) The partial density of states (PDOS) resolved over t_{2g} and e_g orbitals of a Fe atom with the up spin direction and p orbitals in the O atom. The vertical dashed line indicates the Fermi level. For visual clarity, PDOS is multiplied by 3 between −5 and 0 eV.

Table 1 Summary of computed bulk properties of Fe_2O_3 in comparison with previous works. The rhombohedral lattice constant (a) and angle (α), magnetic moment per Fe (μ) and energy gap (E_g)

	a (Å)	α (°)	μ (μ_B)	E_g (eV)
This work	5.47	55.21	4.18	2.25
Other theory[17]	5.47	55.23	4.2	2.3
Experiment	5.43	55.23	4.9	2.0–2.2[a]
				2.6 ± 0.4[b]

[a] Optical gap, see ref. 30. [b] Photoemission, see ref. 31.

nearby Fe and O atoms, suggesting that they are perturbed valence-band states. The topmost β states below the Fermi level consist of mainly d(t_{2g}) orbitals belonging to Fe (short) atoms. (The isosurface of the up-spin β state is displayed in Fig. 2a.) As a result, the nearby two Fe (short) atoms become Fe^{II}. The unoccupied γ state just below the conduction band is mostly d orbitals in Fe (long) atoms (e_g). Therefore, β and γ states resemble the states at the conduction band minimum (CBM) in the bulk.

3.2.2 Iron vacancy (V_{Fe}). Similar to V_O, V_{Fe} also induces the outward (inward) motion of the neighboring oxygen (Fe) atoms

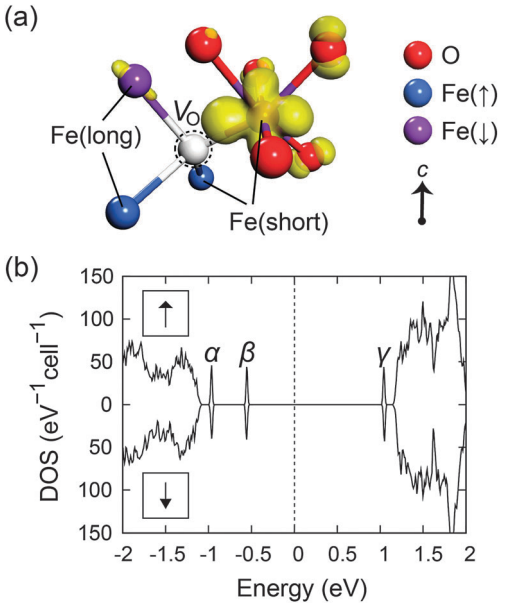

Fig. 2 (a) The local atomic configuration around V_O. The spatial distribution of β state with the spin up is also displayed. (b) The spin-resolved DOS in the presence of V_O. The Fermi level is indicated by the vertical dashed line.

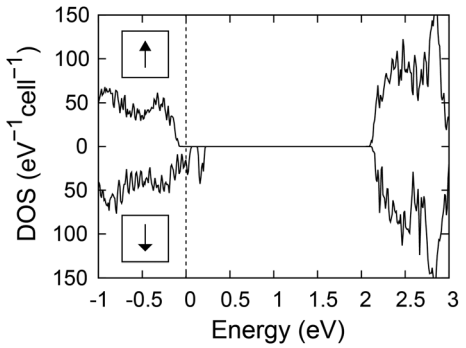

Fig. 3 The spin-resolved DOS in the presence of V_{Fe}. The Fermi level is indicated as the vertical dashed line.

but the extent of atomic relaxation (∼0.2 Å) is larger than for V_O. Fig. 3 shows the spin-resolved DOS when an Fe(↑) atom is removed to form V_{Fe}. It is found that V_{Fe} induces shallow accepter levels in the opposite spin direction of the removed Fe atom close to the valence band maximum (VBM). These states are like the VBM state (a mixed character of O-p and Fe-e_g, see Fig. 1b) but localized within second-nearest neighbors (or ∼4 Å) around the defect site. Because V_{Fe} results in shallow acceptor levels, the p-type character might result with V_{Fe}. If we also apply U correction on O p orbitals with U_{eff} = 6 eV,[32] however, acceptor levels are much more localized to neighboring O p orbitals and form deep levels in the middle of the band gap. This indicates that the localization of acceptor levels may need a more sophisticated approach.

3.2.3 Interstitial oxygen (O_I). In the corundum structure, 2/3 of the octahedral sites surrounded by O atoms are occupied by cations and the remaining 1/3 of the sites are empty. These vacant sites would be suitable for interstitial defects. In addition,

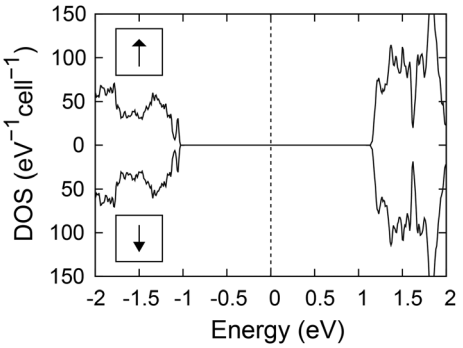

Fig. 4 The spin-resolved DOS in the presence of O_I. The Fermi level is indicated as the vertical dashed line.

O_I is also found in the form of a dumbbell-like split interstitial in some close-packed metal oxides.[33,34] Therefore, we consider both octahedral and split O_I. Furthermore, we carefully examine the magnetic structure of O_I. For the octahedral O_I, the open-shell triplet state is found to be the ground state. In the case of split interstitial, the minimum energy is obtained when the dumbbell points along the $[10\bar{1}1]$ in the closed-shell singlet state, and this structure is more stable than the octahedral O_I by 2.0 eV. Therefore, we discuss the characteristics of this split interstitial in the following.

Due to the large size of O_I, atoms near the interstitial are pushed outward regardless of atomic species. Fig. 4 shows the DOS in the presence of O_I. Because of the closed-shell singlet character, the DOS is spin-symmetric. It is seen that there are no defect levels within the band gap except for shallow levels near the valence edge, indicating that O_I is not charged for most of the range of the Fermi level.

3.2.4 Interstitial iron (Fe_I). We consider both octahedral and tetrahedral interstices as candidate sites for Fe_I. In the case of Fe_I, it is found that the cell-size dependence of Fe_I is more pronounced than other defects, and the 120-atom cell results in a significant overlapping between local atomic distortions and defect states. Therefore, we use the 180-atom supercell by expanding the rhombohedral cell by 3 × 3 × 2. By comparing the total energy, it is found that the octahedral site is more stable than tetrahedral one by 2.0 eV. This is consistent with the conclusion drawn from the experiments and calculations.[10,35]

Considering the octahedral site in the center of the primitive cell as shown in Fig. 5a, two spin configurations, parallel (↑ [↑] ↑) and anti-parallel (↑ [↓] ↑), are possible along the c axis. The spin parallel configuration is more stable than the anti-parallel one over the major charge states (0 to 2+), and we are going to discuss Fe_I with this magnetic configuration in the following.

The two Fe atoms neighboring Fe_I along the c axis relax outward by 0.35 Å, incurring a significant strain field. This necessitates a larger supercell for Fe_I as noted above. The electronic structure in the presence of Fe_I with the spin parallel configuration is shown in Fig. 5b. The spatial distributions of selected defect levels are presented in Fig. 5a. It is seen that defect levels are mostly d orbital with t_{2g} symmetry. Since Fe_I donates two electrons to neighboring Fe atoms along the c axis, three adjacent Fe^{II} atoms are formed including Fe_I.

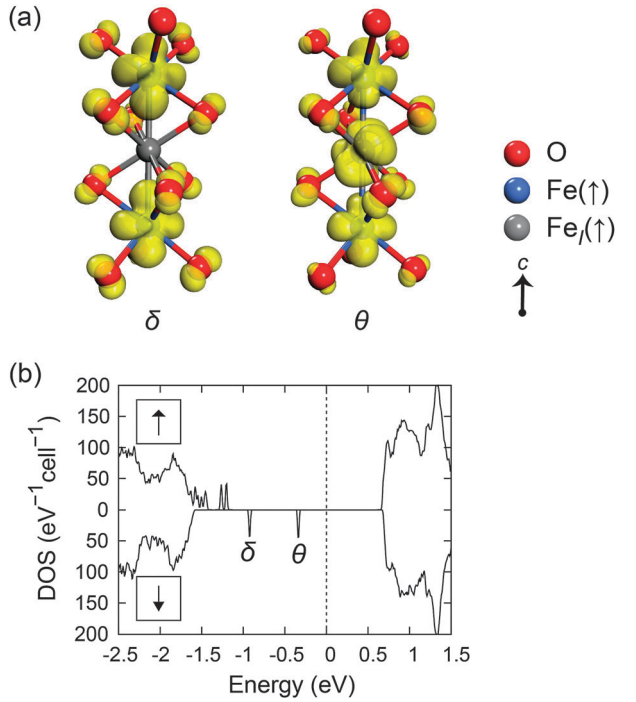

Fig. 5 (a) The local atomic configurations around the Fe interstitial at the octahedral site. The isosurface plots of the states δ and θ marked in (b) are also shown. (b) The spin-resolved DOS in the presence of the octahedral Fe$_I$. The Fermi level is indicated as the vertical dashed line.

3.2.5 Electron polaron (e_p). For some materials, the electron carrier is localized over a few atoms, causing a significant relaxation of surrounding atoms. This type of self-trapped electron corresponds to the electron polaron (e_p). In particular, when the distortion is localized to a region that is less than the lattice constant, it is called the small polaron. Several model studies have explained the conductivity behavior of Fe_2O_3 based on the small polaron model, in which an extra electron presides locally at the Fe atom.[36–38]

To stabilize the electron polaron, we push out O atoms around a specific Fe site slightly and the supercell was charged with one extra electron. After the structural relaxation, the O atoms were displaced from the crystalline site by 0.05–0.12 Å. The electron is then mostly localized at the central Fe atom with d(t_{2g}) character in the minority spin direction, indicative of the small polaron (see Fig. 6). The present calculation is in favorable comparison with the previous Hartree–Fock calculation showing that the electron polaron induces distortions of oxygen atoms by 0.07–0.18 Å.[36] We find that the electron polaron is more stable than the delocalized electron in the conduction band by 0.57 eV. Therefore, we explicitly consider the electron polaron as Fe^{II} defects induced at the host Fe^{III} sites, in addition to the delocalized, extended electron states in the conduction band. On the other hand, we also examined the possibility of the hole polaron but could not identify the localized hole that is more stable than the delocalized one. (The most stable hole polaron configuration was less stable than the delocalized hole by 0.80 eV. When U correction was applied to the oxygen p orbital (see above), the energy difference is reduced to 0.57 eV, but the delocalized state is still more stable.)

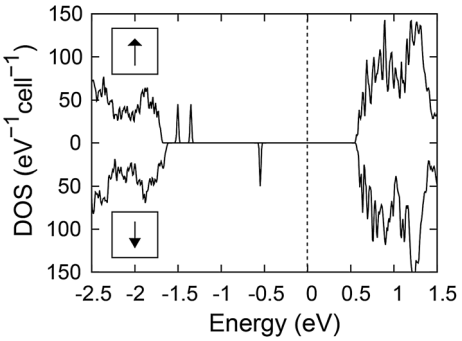

Fig. 6 The density of states in the presence of electron polaron at the Fe(↑) site. The Fermi level is indicated as the vertical dashed line.

3.3 Formation energy of defects

The thermodynamics of point defects can be systematically investigated based on the defect formation energy (E_{for}) which is defined for a defect in the charge state q as follows:

$$E_{for}(\text{defect}, q) = E_{tot}(\text{defect}, q) - E_{tot}(\text{perfect}) + \lambda\mu_X + q(\varepsilon_F + E_{VBM}) \quad (1)$$

where E_{tot} is the total energy of the supercell with or without defects. In eqn (1), μ_X denote the chemical potential of added or removed atomic species X, λ is equal to +1(−1) for the vacancy (interstitial) defect, and ε_F is the Fermi level with respect to the valence band maximum (E_{VBM}).

3.3.1 Finite-size correction. The supercell approach used in the present work requires that the computed E_{for} is well converged with respect to the supercell size. There are several origins that may affect E_{for} in the finite supercell. In the below, we discuss them one by one with the introduction of corresponding correction methods. For the more detailed information, we refer to ref. 39.

Potential alignment correction. Because of the periodic boundary condition (PBC), the average Coulomb potential is always constrained to be zero. Therefore, the potential change near the defect site is balanced by a constant shift (ΔV) even in the case of neutral defects. This constant shift affects the position of VBM and E_{for} of the charged defects in eqn (1). This is corrected by adding $q\Delta V$ to E_{for} in eqn (1), and this is called the potential alignment correction (PA). One can estimate ΔV by comparing the average Coulomb potential at the oxygen core in the bulk-like region in the neutral defective cell with those in perfect cells.

Spurious Coulomb interaction. Due to PBC, the interaction between repeated defects is unavoidable. In particular, when the defects are charged, neutralizing background charges are added for the compatibility with PBC, and Coulomb interactions between various charge sources should be systematically corrected. Makov and Payne (MP) proposed a correction scheme based on a molecule-like charged species repeated in cubic supercells with a length of L:[40]

$$E_{MP} = \frac{q^2\alpha}{2\varepsilon^0 L} + \frac{2\pi qQ}{3\varepsilon^0 L^3} + O(L^{-5}) \quad (2)$$

where q, ε^0, α, and Q are the defect charge, static dielectric constant, Madelung constant, and second moment of defect charge distribution, respectively. In eqn (2), the first term represents the monopole–monopole interaction between repeated localized charges within the uniform background charge, and the second term corresponds to the monopole–quadrupole interaction. In the present work, we consider only the monopole–monopole term. The static dielectric constant is computed using the density functional perturbation theory as implemented in VASP and we assumed an isotropic dielectric medium by averaging diagonal components of the dielectric tensor (23.3 in comparison with the experimental value of 22.9 (ref. 41)). In addition, Lany and Zunger (LZ) recently proposed a different scheme where the monopole–monopole correction in MP is scaled by a factor of about 0.65, and we also test this approach.[42]

In order to choose an efficient scheme with the minimal supercell size, we applied the above methods to E_{for} of V_O^{2+} with respect to various supercells ranging over 80, 120, 180, 270, 360, and 640 atoms. Fig. 7 displays the convergence of E_{for} with respect to the cell-size parameter L which is set to the cubic root of supercell volume. Various schemes are noted as PA-only (PA), MP with or without PA (MPPA and MP, respectively), and Lany–Zunger (LZ) types. In order to account for the unknown remaining size effects, the computed data are fitted using $\frac{a}{L}+\frac{b}{L^3}+c$, where a, b, and c are fitting parameters. We did not include the results with 80 atoms in fitting because a large error is expected due to the small cell size. In Fig. 7, it is noted that all fitting functions converge to the same value at the limit of infinite cell size ($L^{-1} \rightarrow 0$), which means that the converged value of 1.2 eV can be regarded as the reference E_{for} corresponding to the truly isolated defect. With this reference value, it is seen that MPPA approach produces the best estimate for the given finite cell size. In the following calculations, therefore, we compute E_{for} with 120-atom cell together with MPPA scheme, as marked by a dashed circle in Fig. 7. (For Fe_I, 180-atom cell is used.) Although small errors of $\lesssim$0.05 eV may remain, this would not change the main conclusions.

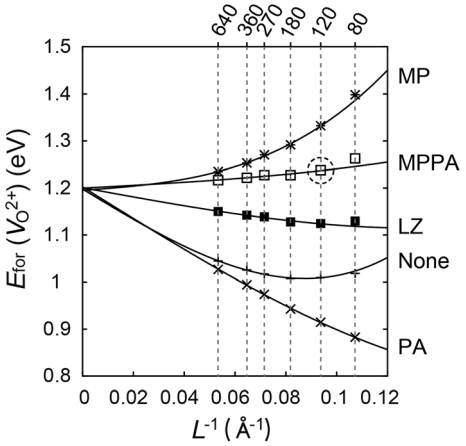

Fig. 7 The convergence of defect formation energy (E_{for}) of V_O^{2+} with respect to the supercell size. The numbers of atoms in the non-defective supercell are indicated in the top. The abscissa indicates the inverse cubic root of the supercell volume. The correction schemes are Makov–Payne (MP), potential alignment correction (PA), Lany–Zunger (LZ), and MP together with PA (MPPA). The solid lines are fit to the form of $\frac{a}{L}+\frac{b}{L^3}+c$.

3.3.2 Oxygen chemical potential. As shown in eqn (1), E_{for} requires the information on μ_O or μ_{Fe}, chemical potentials of constituent elements. Since these two parameters are constrained by the free energy of Fe_2O_3, only one variable is independent. Here, we discuss the range of oxygen chemical potential (μ_O) assuming that the material is in equilibrium with oxygen gas.

When Fe_2O_3 is in equilibrium with oxygen gas at a certain temperature T and pressure p, the corresponding μ_O is given by[43]

$$\mu_O = \frac{1}{2}\mu_{O_2}(T,p) \tag{3}$$

where μ_{O_2} is the chemical potential of the O_2 molecule. The chemical potential of a gas phase is related to the value at the standard pressure as follows:

$$\mu_{O_2}(T,p) = \mu_{O_2}(T,p^\circ) + k_B T \ln\left(\frac{p}{p^\circ}\right) \tag{4}$$

In addition,

$$\mu_{O_2}(T, p^\circ) = \Delta H - T\Delta S + \mu_{O_2}(0\ \text{K}, p^\circ) \tag{5}$$

where ΔH and ΔS are the enthalpy and entropy changes per molecule between T and 0 K at the standard pressure, respectively, and are available from thermochemical tables.[44] In eqn (5), $\mu_{O_2}(0\ \text{K}, p^\circ)$ is equal to $E_{\text{tot}}(O_2)$. Because of the well-known overbinding problem in small molecules within GGA, we use the experimental value of 5.23 eV for the binding energy of the O_2 molecule.[45] By subtracting this from 2× atomic energy of oxygen, we get −9.04 eV for $\mu_{O_2}(0\ \text{K}, p^\circ)$. This is defined as the oxygen-rich limit. We note that the oxidation enthalpy of magnetite to hematite ($2Fe_3O_4 + 1/2O_2 \rightarrow 3Fe_2O_3$) is improved when the experimental binding energy of O_2 is used (−2.47 and −2.06 eV with and without the correction of O_2 binding energy, respectively, in comparison with the experimental data of −2.52 eV.)

As the oxygen pressure is decreased, oxygen-deficiency in Fe_2O_3 increases and eventually Fe_2O_3 reaches equilibrium with Fe_3O_4. This corresponds to the metal-rich limiting condition. The oxygen chemical potential under this condition is given by the following relation:

$$\mu_O^{\text{Fe-rich}} = 3G(Fe_2O_3;\ T,\ p) - 2G(Fe_3O_4;\ T,\ p) \tag{6}$$

where G is the Gibbs free energy. Neglecting the contribution by the free energy change of solids between different pressures and assuming 0 K in eqn (6), the Gibbs free energy can be approximated as the total energy of each material:

$$\begin{aligned}\mu_O^{\text{Fe-rich}} &\simeq 3G(Fe_2O_3; 0\ \text{K}, p^\circ) - 2G(Fe_3O_4; 0\ \text{K}, p^\circ)\\ &\simeq 3E_{\text{tot}}(Fe_2O_3) - 2E_{\text{tot}}(Fe_3O_4)\end{aligned} \tag{7}$$

We calculate the total energy of Fe_3O_4 following the structural and magnetic configuration in ref. 46, and the resulting oxygen chemical potential in the Fe-rich limit is computed to be −6.99 eV.[47]

3.3.3 Charge transition levels. Based on the defect formation energies, the charge transition diagrams can be plotted.

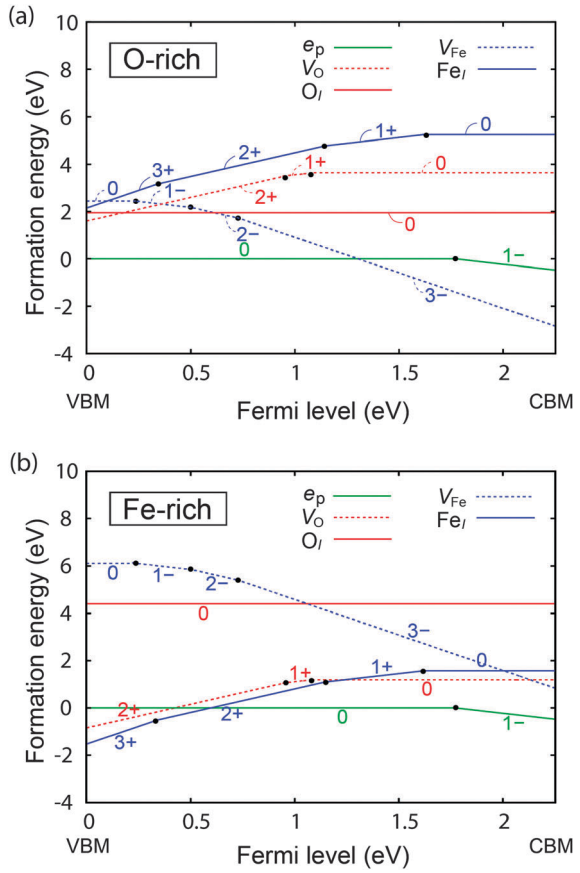

Fig. 8 Defect formation energies at the most stable charge states are given as a function of Fermi level in (a) O-rich and (b) Fe-rich limits. The solid dots indicate charge transition levels.

Fig. 8 shows E_{for} as a function of the Fermi level under the oxygen-rich and Fe-rich conditions. For convenience, only the most stable charge states are plotted and the solid dots indicate the transition levels at which two different charge states cross. For e_p, 0 and 1− charge states correspond to Fe^{III} and Fe^{II} valence states for the host Fe site, respectively.

In the oxygen-rich limit where μ_O is equal to $\frac{1}{2}E_{tot}(O_2)$ (see above), the negatively charged V_{Fe} is found to be the most stable over a wide range of the Fermi level. These ionized cation vacancies may give rise to p-type conductivity by creating holes in the valence bands. On the other hand, under the Fe-rich condition in Fig. 8b, V_O and Fe_I are equally probable. However, $V_O(1+/0)$ transition level (1.08 eV) is significantly deeper than $Fe_I(1+/0)$ (1.62 eV) with respect to the polaron formation level at 1.77 eV. This means that Fe_I, rather than V_O, is the source of the electron carrier.

4 Discussion

The defect concentration $D_X(q)$ of defect X with charge q is given by:[49]

$$\frac{D_X(q)}{n_X} = \frac{\exp[-E_{for}(X(q))/k_B T]}{1 + \sum_{X'}\sum_{q'}\exp[-E_{for}(X'(q'))/k_B T]} \quad (8)$$

where n_X and k_B are the concentration of possible lattice sites for the defect X and the Boltzmann constant, respectively. Since the defect densities are usually much smaller than 1, eqn (8) can be approximated as

$$\frac{D_X(q)}{n_X} \simeq \exp[-E_{for}(X(q))/k_B T] \quad (9)$$

In the case of the electron polaron, the possible defect sites are Fe atoms. The concentrations of delocalized electrons and holes (n and p, respectively) are evaluated by the Fermi–Dirac distribution and DOS ($D(\varepsilon)$):

$$n = \int_{E_{CBM}}^{\infty} D(\varepsilon) f_{FD}(\varepsilon, \varepsilon_F) d\varepsilon \quad (10)$$

$$p = \int_{-\infty}^{E_{VBM}} D(\varepsilon)(1 - f_{FD}(\varepsilon, \varepsilon_F)) d\varepsilon, \quad (11)$$

where $f_{FD}(\varepsilon, \varepsilon_F)$ is the Fermi–Dirac distribution function with the Fermi level of ε_F. We approximate the integration of given function as the summation over 30 × 30 × 30 k-point mesh within the first Brillouin zone. The Fermi level is determined by the condition of charge neutrality:

$$\sum_X \sum_q q \cdot D_X(q) - n + p = 0 \quad (12)$$

In the following, we will discuss the density of intrinsic point defect under various conditions.

4.1 Defect density and non-stoichiometry at high temperatures

Fig. 9a is the Brouwer diagram showing the equilibrium density of major defects with respect to μ_O or p_{O_2} at 1373 K (or 1100 °C). We note that Fe_2O_3 is paramagnetic at 1373 K which is well above the Néel temperature (960 K). The defect formation energies could be affected by the change in magnetic ordering, but it is neglected in the present study. The corresponding Fermi level is shown in Fig. 9b. Since the Fermi level is mostly fixed near the band gap center, only one charge state appears for each defect.

In Fig. 9a, the defect densities are insignificant when p_{O_2} is above 1 atm and Fe_2O_3 becomes an intrinsic semiconductor. Therefore, the density of electron polaron and hole are almost identical. (Since the formation of electron polaron is much favorable than the delocalized electron in the conduction band, the density of delocalized electron is negligible.) Near the metal-rich condition ($p_{O_2} < 10^{-2}$ atm), on the other hand, the density of positively ionized V_O and Fe_I increases considerably, making Fe_2O_3 an n-type semiconductor.

Using the calculated defect concentrations, the compositional ratio between cation and anion as well as oxygen deficiency can be determined with respect to p_{O_2}. In Fig. 10, we compare the oxygen deficiency (δ in $Fe_2O_{3-\delta}$) at various temperatures with experimental data in ref. 11 and excellent agreements are found. In Fig. 10, we find that the slope in $\log\delta - \log p_{O_2}$ changes from 1/2 at high p_{O_2} to 1/4 at low p_{O_2}. This is because the dominant defect types are V_O and Fe_I at high and low p_{O_2}, respectively.

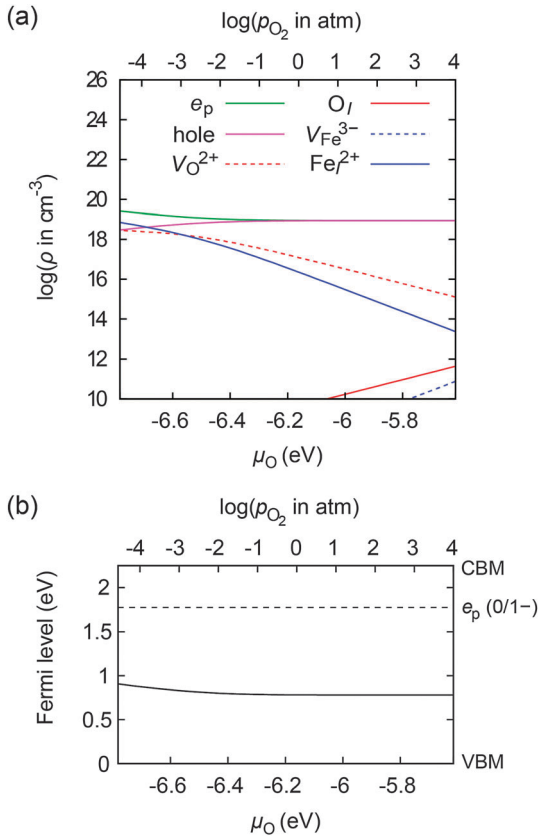

Fig. 9 (a) Brouwer diagram for the equilibrium condition at 1373 K, and (b) corresponding Fermi level are shown. The polaron formation level (e_p(0/1−)) is shown as a horizontal dashed line.

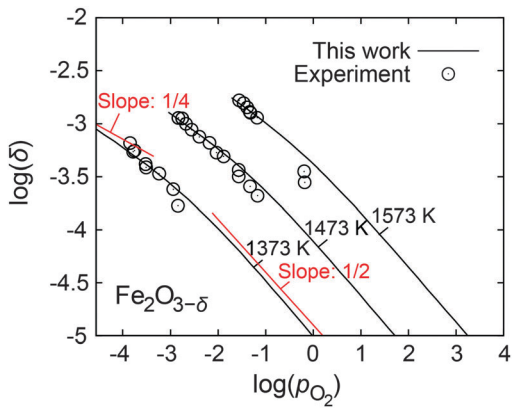

Fig. 10 Deviation from the stoichiometry (δ) with respect to the oxygen partial pressure (p_{O_2}). The experimental data are obtained from ref. 11.

From the experimental data with the slope close to 1/2, it was claimed that V_O is the dominant defect[11] but it is confirmed in the present study that Fe_I is equally dominant.

4.2 Quenched condition

Even though Fe_2O_3 is synthesized at high temperatures, the material is mainly used under ambient conditions. While light particles such as electrons or holes reach the equilibrium states rapidly, the smaller diffusivity of ions freeze the density of ionic defects when the sample is quenched to the room temperature. Nevertheless, the ratio between different charge states should be equilibrated:

$$\frac{D_X(q)}{D_X(q')} = \frac{\exp[-E_{\text{for}}(X(q))/k_B T]}{\exp[-E_{\text{for}}(X(q'))/k_B T]} \quad (13)$$

With the total number of a certain defect type fixed to the value equilibriated at high temperatures, the Fermi level and detailed charge distributions are determined by eqn (12) and (13). Fig. 11a and b show the Fermi level and the defect densities with respect to the chemical potential under the high-temperature growth conditions. As the intrinsic carrier concentration is significantly reduced at the room temperature, the Fermi level is mainly determined by the dominant charge defects. Therefore, the variations in the defect concentrations with respect to μ_O directly affect the Fermi level, resulting in large variation as shown in Fig. 11a. However, the Fermi level is pinned to ~1.5 eV below CBM, which corresponds to the formation of the electron polaron. Such Fermi-level pinning below CBM may negatively affect the efficiency when Fe_2O_3 is used as the photoanode where large band bending is utilized to drive the photo-generated holes towards the surface.[1]

The corresponding defect densities are shown in Fig. 11b. It is notable that the neutral V_O is the most stable in comparison

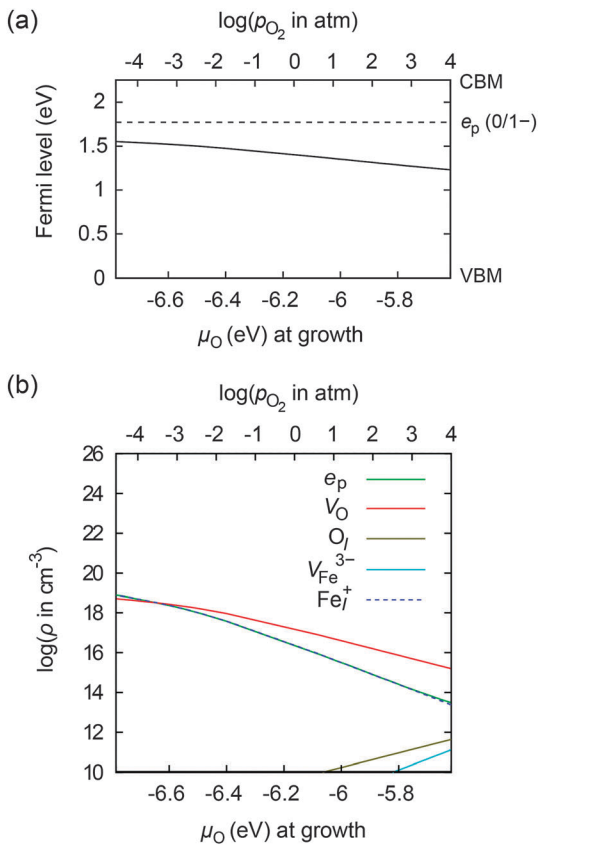

Fig. 11 (a) The Fermi level and (b) the Brouwer diagram when Fe_2O_3 grown at 1373 K is quenched under the ambient conditions. The abscissa indicates the oxygen chemical potential under the growth conditions.

with charged V_O over a wide range of μ_O, which indicates that the oxygen vacancy acts as a deep donor and does not contribute to the n-type conductivity. It is found that the electron polaron is mostly contributed by ionized Fe_I defects.

5 Conclusion

In summary, we investigated the native point defects in Fe_2O_3 using *ab initio* methods based on the GGA + *U* formalism. We considered vacancies and interstitials of Fe and O atoms and determined the formation energies and charge transition levels of each defect type in the isolated limit. It was found that Fe_I and V_{Fe} form shallow donor and acceptor levels, respectively, and therefore these are the defect types that may introduce carriers under ambient conditions. We determined the oxygen deficiency under high-temperature equilibrium conditions and an excellent agreement with the previous experiment was found. In the quenched condition, we found that the Fermi levels are pinned at $\sim$0.5 eV below the conduction band minimum, which may limit the performance of Fe_2O_3 as photoanodes of solar water-splitting cells. We found that V_O is neutral under ambient conditions and Fe_I is responsible for electron carriers. Having established the fundamental electronic character of point defects, we believe that the present results will provide useful information for optimizing the material properties of Fe_2O_3.

Acknowledgements

We thank Ki Tae Nam for motivating us into this work. This research was supported by the EDISON program (NRF-2012M3C1A6035307). The computation was carried out at the KISTI supercomputing center (KSC-2012-C3-20).

References

1 K. Sivula, F. L. Formal and M. Grätzel, *ChemSusChem*, 2011, **4**, 432–449.
2 Á. Valdés, J. Brillet, M. Grätzel, H. Gudmundsdóttir, H. A. Hansen, H. Jónsson, P. Klüpfel, G.-J. Kroes, F. L. Formal, I. C. Man, F. S. Martins, J. K. Nørskov, J. Rossmeisl, K. Sivula, A. Vojvodic and M. Zäch, *Phys. Chem. Chem. Phys.*, 2012, **14**, 49–70.
3 T.-Y. Yang, H.-Y. Kang, U. Sim, Y.-J. Lee, J.-H. Lee, B. Koo, K. T. Nam and Y.-C. Joo, *Phys. Chem. Chem. Phys.*, 2013, **15**, 2117–2124.
4 Y. Ling, G. Wang, D. A. Wheeler, J. Z. Zhang and Y. Li, *Nano Lett.*, 2011, **11**, 2119–2125.
5 A. Kay, I. Cesar and M. Gräzel, *J. Am. Ceram. Soc.*, 2006, **128**, 15714–15721.
6 Y. Ling, G. Wang, J. Reddy, C. Wang, J. Z. Zhang and Y. Li, *Angew. Chem.*, 2012, **51**, 4074–4079.
7 G. Wang, Y. Ling and Y. Li, *Nanoscale*, 2012, **4**, 6682–6691.
8 H. Wang, L. Jia, P. Bogdanoff, S. Fiechter, H. Möhwald and D. Shchukin, *Energy Environ. Sci.*, 2013, **6**, 799–804.
9 G. Wang, H. Wang, Y. Ling, Y. Tang, X. Yang, R. C. Fitzmorris, C. Wang, J. Z. Zhang and Y. Li, *Nano Lett.*, 2011, **11**, 3026–3033.
10 R. F. G. Gardner, F. Sweett and D. W. Tanner, *J. Phys. Chem. Solids*, 1963, **24**, 1187–1351.
11 R. Dieckmann, *Philos. Mag. A*, 1993, **68**, 725–745.
12 K. Hoshino and N. L. Peterson, *J. Phys. Chem. Solids*, 1985, **46**, 1247–1254.
13 K. H. Kim, S. H. Lee and J. S. Choi, *J. Phys. Chem. Solids*, 1985, **46**, 331–338.
14 B. M. Warnes, F. F. Aplan and G. Simkovich, *Solid State Ionics*, 1984, **12**, 271–276.
15 O. Warschkow, D. E. Ellis, J. Hwang, N. M. Hadavi and T. O. Mason, *J. Am. Ceram. Soc.*, 2002, **85**, 213–220.
16 C. R. A. Catlow, J. Corish, J. Hennessy and W. C. Mackrodt, *J. Am. Ceram. Soc.*, 1988, **71**, 42–49.
17 P. Liao and E. A. Carter, *Phys. Chem. Chem. Phys.*, 2011, **13**, 15189–15199.
18 N. J. Mosey, P. Liao and E. A. Carter, *J. Chem. Phys.*, 2008, **129**, 014103.
19 N. C. Wilson and S. P. Russo, *Phys. Rev. B: Condens. Matter Mater. Phys.*, 2009, **79**, 094113.
20 G. Kresse and J. Furthmuller, *Phys. Rev. B: Condens. Matter Mater. Phys.*, 1996, **54**, 11169–11186.
21 P. E. Blochl, *Phys. Rev. B: Condens. Matter Mater. Phys.*, 1994, **50**, 17953–17979.
22 S. L. Dudarev, G. A. Botton, S. Y. Savrasov, C. J. Humphreys and A. P. Sutton, *Phys. Rev. B: Condens. Matter Mater. Phys.*, 1998, **57**, 1505–1509.
23 F. J. Morin, *Phys. Rev.*, 1951, **83**, 1005–1010.
24 M. Catti and G. Valerio, *Phys. Rev. B: Condens. Matter Mater. Phys.*, 1995, **51**, 7441–7450.
25 G. Rollmann, A. Rohrbach, P. Entel and J. Hafner, *Phys. Rev. B: Condens. Matter Mater. Phys.*, 2004, **69**, 165107.
26 Z. D. Pozun and G. Henkelman, *J. Chem. Phys.*, 2011, **134**, 224706.
27 B. Gilbert, C. Frandsen, E. R. Maxey and D. M. Sherman, *Phys. Rev. B: Condens. Matter Mater. Phys.*, 2009, **79**, 035108.
28 Y. Ma, P. D. Johnson, N. Wassdahl, J. Guo, P. Skytt, J. Nordgren, S. D. Kevan, J.-E. Rubensson, T. B. Oske and W. Eberhardt, *Phys. Rev. B: Condens. Matter Mater. Phys.*, 1993, **48**, 2109–2111.
29 We aligned *x*, *y*, and *z* axis such that they nearly point to neighboring oxygen atoms from Fe at the octahedron center. (In VASP, the wave functions are decomposed into spherical harmonics according to *x*, *y*, and *z* axis, rather than lattice vectors.).
30 P. Merchant, R. Collins, R. Kershaw, K. Dwight and A. Wold, *J. Solid State Chem.*, 1979, **27**, 307–315.
31 R. Zimmermann, P. Steiner, R. Claessen, F. Reinert, S. Hufner, P. Blaha and P. Dufek, *J. Phys.: Condens. Matter*, 1999, **11**, 1657–1682.
32 R. Pentcheva and W. E. Pickett, *Phys. Rev. B: Condens. Matter Mater. Phys.*, 2006, **74**, 035112.
33 A. A. Sokol, A. Walsh and C. R. A. Catlow, *Chem. Phys. Lett.*, 2010, **492**, 44–48.

34 T. Brudevoll, E. A. Kotomin and N. E. Christensen, *Phys. Rev. B: Condens. Matter Mater. Phys.*, 1996, **53**, 7731–7735.
35 S. Hallström, L. Höglund and J. Ågren, *Acta Mater.*, 2011, **59**, 53–60.
36 K. M. Rosso, D. M. A. Smith and M. Dupuis, *J. Chem. Phys.*, 2003, **118**, 6455.
37 F. J. Morin, *Phys. Rev.*, 1954, **93**, 1195–1199.
38 A. J. Bosman and H. J. van Daal, *Adv. Phys.*, 2006, **19**, 1–117.
39 H.-P. Komsa, T. T. Rantala and A. Pasquarello, *Phys. Rev. B: Condens. Matter Mater. Phys.*, 2012, **86**, 045112.
40 G. Makov and M. C. Payne, *Phys. Rev. B: Condens. Matter Mater. Phys.*, 1995, **51**, 4014–4022.
41 S. Onari, T. Arai and K. Kudo, *Phys. Rev. B: Solid State*, 1977, **16**, 1717–1721.
42 S. Lany and A. Zunger, *Phys. Rev. B: Condens. Matter Mater. Phys.*, 2008, **78**, 235104.
43 K. Reuter and M. Scheffler, *Phys. Rev. B: Condens. Matter Mater. Phys.*, 2001, **65**, 035406.
44 P. J. Linstrom and W. G. Mallard, *NIST Chemistry WebBook, NIST Standard Reference Database Number 69*, National Institute of Standards and Technology, Gaithersburg, MD, 2011, http://webbook.nist.gov.
45 L. Wang, T. Maxisch and G. Ceder, *Phys. Rev. B: Condens. Matter Mater. Phys.*, 2006, **73**, 195107.
46 H.-T. Jeng, G. Y. Guo and D. J. Huang, *Phys. Rev. B: Condens. Matter Mater. Phys.*, 2006, **74**, 195115.
47 In the case of Fe_3O_4, it is known that 3.61 eV is appropriate as U_{eff}.[48] When this value is used, $\mu_O^{Fe\text{-}rich}$ is calculated to be −7.20 eV.
48 H.-T. Jeng, G. Y. Guo and D. J. Huang, *Phys. Rev. Lett.*, 2004, **93**, 156403.
49 S. Kasamatsu, T. Tada and S. Watanabe, *Solid State Ionics*, 2011, **183**, 20–25.

